

Learning Parameter Sharing with Tensor Decomposition and Sparsity

Cem Üyük¹ Mike Lasby² Mohamed Yassin² Utku Evci^{*3} Yani Ioannou^{*2}

Abstract

Large neural networks exhibit exceptional performance across numerous tasks, yet their considerable size often hinders deployment on resource-constrained systems. While various model compression strategies have been well studied, parameter sharing remains underexplored. In this paper, we introduce **Fine-grained Parameter Sharing (FiPS)**, a novel algorithm that leverages parameter sharing, tensor decomposition, and sparsity to effectively compress large-scale Vision Transformers (ViTs) and Large Language Models (LLMs). FiPS employs a shared basis and sparse factors to represent neurons across multi-layer perceptron (MLP) modules, where initialization is guided by Singular Value Decomposition (SVD) and subsequent optimization is conducted through block-wise reconstruction error minimization. Experimental results show that FiPS reduces the parameter budget of MLP modules by 50–75% for DeiT-B and Swin-L and by 40–50% for various Gemma-2 and Llama-3 models while maintaining ViT model accuracy within 1% pt. of the original and LLM perplexity with negligible degradation.

1 Introduction

Over the past decade, large neural networks have delivered impressive performance by scaling datasets and model sizes. However, this trend has introduced substantial computational, memory, and storage burdens, highlighting the need for efficient model compression to reduce overhead and enable deployment on resource-constrained devices such as mobile phones and embedded systems. In response, researchers have explored various strategies, including tensor decomposition, quantization, distillation, sparsity, parameter sharing, and adaptive computing methods (Cheng et al., 2020). While most of these techniques are well-studied and widely adopted, parameter sharing has received relatively less attention.

¹Technical University of Munich, ²University of Calgary, ³Google DeepMind. Correspondence to: Cem Üyük <uyuc@in.tum.de>, Utku Evci <evcu@google.com>.

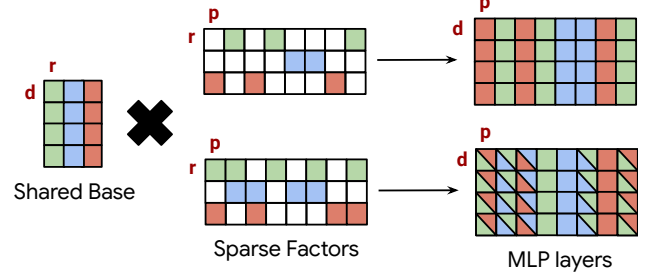


Figure 1: **Fine-grained Parameter Sharing (FiPS)** employs a shared basis for the sparse weight matrices in the Fully Connected (FC) layers of Multi-Layer Perceptron (MLP) modules across transformer blocks. This approach is detailed in § 2 and § 3.

Sharing parameters across multiple neural network layers can theoretically reduce memory usage and improve cache efficiency, potentially accelerating execution. Building on this idea, several previous works have investigated reusing entire Transformer blocks within the network architecture (Lan et al., 2020; Takase & Kiyono, 2023; Lin et al., 2023), yielding more efficient models. Although directly sharing unmodified weights across layers is promising, we hypothesize that a more fine-grained approach could lead to better compression.

Consequently, our focus shifts to sharing neurons across layers, achieved by using a shared basis, where each neuron is computed as a linear combination of this basis. Moreover, we find that sparsity in the projection matrix is essential for the approach to be effective. This insight leads to our novel parameter sharing algorithm, **Fine-grained Parameter Sharing (FiPS)**¹, which we demonstrate effectively compresses large Vision Transformers (ViTs) and Large Language Models (LLMs)². Our contributions include:

- Neuron sharing is demonstrated as feasible by employing sparse tensor decomposition in the Multi-Layer Perceptron (MLP) modules.
- Configurations for sharing neurons are systematically investigated, with a focus on effective concatenation strategies for MLPs.

¹The source code is available at <https://github.com/cemuyuk/FiPS>.

²All model links are available in appendix B.1.

- Building on these findings, FiPS is introduced as a method that leverages Singular Value Decomposition (SVD) (i.e., $\mathbf{W} = \mathbf{U}\Sigma\mathbf{V}^\top$) to initialize compressed models and refines the decomposed parameters through block-wise optimization.
- Applying FiPS (with both unstructured and structured sparsity) to DeiT-B (Touvron et al., 2021) and Swin-L (Liu et al., 2021) reduces MLP module sizes to 25–40% of the original, with less than a 1% point drop in accuracy.
- The MLP modules of Gemma-2 (2B, 9B) (Team et al., 2024) and Llama-3 (3B, 8B) (Grattafiori et al., 2024) are compressed by 40-50%, while maintaining perplexity with negligible degradation.

In the following, we discuss how parameter sharing is facilitated by tensor decomposition and sparsity in tandem, introduce FiPS, present the results, and ablate key components.

2 Parameter Sharing Through Sparse Tensor Decomposition

Consider a weight matrix, $\mathbf{W} \in \mathbb{R}^{d \times p}$, which projects feature vectors from a d -dimensional space to a p -dimensional space, with neurons represented by the columns of \mathbf{W} . Our objective is to share weights among a subset of these p neurons, reducing the number of unique neurons to $r < p$. In other words, only r columns of \mathbf{W} will contain unique values. These r unique neurons are represented using a lookup table (basis matrix) $\mathbf{U} \in \mathbb{R}^{d \times r}$. The original matrix \mathbf{W} is then reconstructed by mapping each of its p columns to an r -dimensional one-hot vector via a projection matrix $\mathbf{V} \in \mathbb{R}^{r \times p}$, i.e., $\mathbf{W} = \mathbf{U}\mathbf{V}$. This "one-hot" approach is illustrated in the upper part of Figure 1.

However, limiting the number of unique neurons to r constrains the representational capacity of \mathbf{W} . To address this limitation, we can increase the number of non-zero elements in \mathbf{V} , effectively creating combinations of the basis neurons and generating a significantly larger set of unique neuron representations, as shown in the lower part of Figure 1.

Thus far, we have focused on sharing neurons within a single weight matrix \mathbf{W} . This approach can be readily extended to multiple weight matrices $\mathbf{W}_1, \dots, \mathbf{W}_N$. Specifically, fine-grained parameter sharing across multiple layers can be achieved by expanding the size of the projection matrix \mathbf{V} and the shared basis \mathbf{U} .

The aforementioned approach can be viewed as a low-rank decomposition of the matrix \mathbf{W} , where the first factor \mathbf{U} is shared and the second factor \mathbf{V} is sparse. Therefore, existing low-rank decomposition techniques can be employed to obtain an optimal shared orthogonal basis, and sparsity in the projection matrices can be induced using current pruning and sparse training methods.

In the following sections, we utilize a pre-trained DeiT-B model (comprising 12 encoder blocks, each containing one MLP module, pre-trained on ImageNet-1k (Deng et al., 2009)) to investigate the optimal strategy for tying multiple layers within this framework. We focus on the model’s MLP modules, which typically contain most parameters (e.g., 70.5% of all parameters in Gemma-2-9B). Each module comprises two fully connected layers with dimensions $\mathbb{R}^{d \times p}$ and $\mathbb{R}^{p \times d}$, respectively, where $p = 4d$. In the following and in the context of FiPS, the parameter budget represents the fraction of retained parameters after truncated SVD minus the nonzero parameters preserved in the decomposed factors after sparsification. For example, a 25% budget means one-fourth of the original module’s parameters remain nonzero.

2.1 Optimal Sparsity for Tensor Decomposition

Before implementing parameter sharing through shared bases, we decompose individual FC layers using a truncated SVD under a 25% parameter budget. Subsequently, we introduce sparsity by zeroing out low-magnitude values. Specifically, we examine sparsity induction in: (1) \mathbf{U} , (2) \mathbf{V} , and (3) both \mathbf{U} and \mathbf{V} . Throughout this process, we vary the sparsity levels of the matrices while maintaining a constant total number of non-zero parameters. The resulting reconstruction errors are presented in Figures 2a and 2b. Our observations indicate that optimal reconstruction errors are achieved at sparsity levels between 60% and 80%, particularly when sparsity is applied to the larger factor matrix \mathbf{V} . We attribute this effectiveness to the higher redundancy in larger matrices, facilitating more efficient pruning.

2.2 Weight Concatenation and Sharing Dimensions

Next, we investigate parameter sharing across multiple layers within a network. The analysis focuses on four FC layers derived from two distinct MLP modules, exploring various concatenation strategies to determine the optimal approach for constructing a shared basis.

To achieve this, the parameters of the second FC layer in each MLP module are transposed, representing each layer with a weight matrix $\mathbf{W} \in \mathbb{R}^{d \times 4d}$, and four distinct concatenation configurations are examined:

- (I) **Full Long-Axis Concatenation:** Concatenate all matrices along the longer axis to form $\mathbf{W}_s \in \mathbb{R}^{d \times 16d}$.
- (II) **Module-wise Long and Inter-module Short Concatenation:** Concatenate FC layers within the same module along the longer axis, and then concatenate different modules along the shorter axis, resulting in $\mathbf{W}_s \in \mathbb{R}^{2d \times 8d}$.
- (III) **Module-wise Short and Inter-module Long Concatenation:** Contrary to (II), concatenate FC layers within the same module along the shorter axis, and then

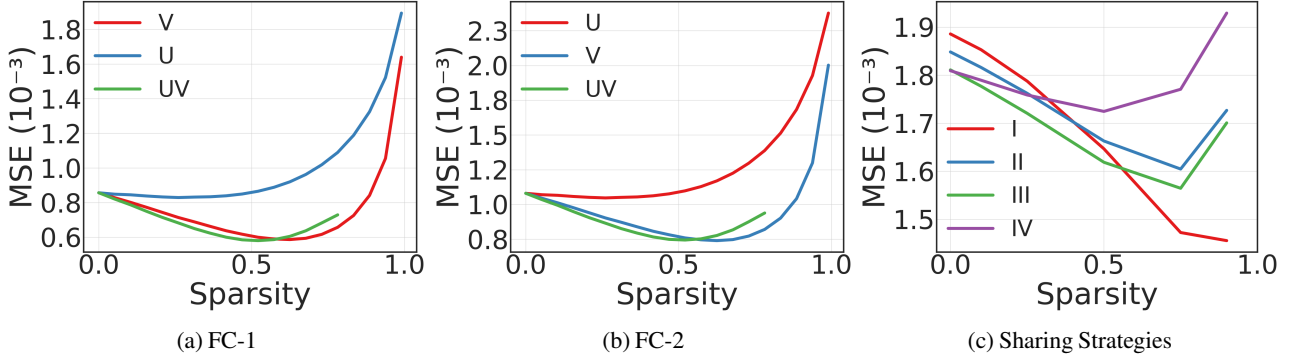


Figure 2: **Initial Experiments.** Reconstruction error when inducing sparsity on different factors of the low-rank decomposition for (a) FC-1 and (b) FC-2 layers under a 25% parameter budget. Higher sparsity in larger factors (V) enables a higher rank and lower reconstruction error. (c) Mean reconstruction error across four FC layers under various parameter sharing schemes. See § 2.2 for a description of each strategy.

concatenate different modules along the longer axis, yielding $\mathbf{W}_s \in \mathbb{R}^{2d \times 8d}$.

- (IV) **Full Short-Axis Concatenation:** Concatenate all layers along the shorter axis to obtain $\mathbf{W}_s \in \mathbb{R}^{4d \times 4d}$.

For each concatenated matrix \mathbf{W}_s , we perform truncated SVD, retaining the top r singular vectors. The resulting right singular vector matrix \mathbf{V} is then sparsified by preserving the highest-magnitude entries, an approach shown in § 2.1 to be optimal for reconstruction. Finally, we reconstruct the parameters using the shared basis and report the mean squared error (MSE) in Figure 2c.

Our experiments reveal that concatenating weights along the longer dimension consistently yields the lowest reconstruction errors, particularly at higher sparsity levels. Therefore, we adopt this concatenation strategy for all subsequent experiments, consistently concatenating the FC layers of MLP modules along their larger dimension.

2.3 Parameter Sharing Across Layers

This section examines the redundancy and interdependencies among different MLP modules to identify optimal groupings for parameter sharing. We begin by decomposing individual modules with a rank of $r = 180$ and plot the resulting MSE in the bottom section of Figure 3a. The data indicate a nearly monotonic increase in error with respect to the module index, suggesting that deeper modules in the network require greater capacity.

Subsequently, we pair two MLP modules from distinct blocks (i and j) and assign them a shared basis \mathbf{U} . This parameter sharing scheme reduces the overall parameter count but increases the MSE for each block. In this shared configuration, the MSE for block i is denoted as $MSE_{i,j}$. In Figure 3a, we

illustrate the average MSE increase between blocks i and j as:

$$MSE_{i,j}^{\uparrow} = \frac{(MSE_i - MSE_{i,j}) + (MSE_j - MSE_{j,i})}{2}.$$

Empirical results demonstrate that adjacent blocks exhibit the smallest increase in MSE, thereby motivating the grouping of consecutive layers for parameter sharing.

We further explore the optimal number of MLP modules per group. Increasing the group size allows for a higher rank within the shared basis \mathbf{U} , as depicted in Figure 3b. This effect is particularly pronounced when sparsity is applied to the factor \mathbf{V} . However, a higher rank does not universally translate to improved accuracy, as the shared basis must adequately represent a larger number of parameters. As shown in Figure 3c, the highest post-compression accuracy is achieved when parameters are shared across four consecutive MLP modules.

3 Fine-grained Parameter Sharing

Experiments in the previous section motivate and guide us in developing FiPS, an efficient parameter sharing algorithm enabled by sparse tensor decompositions that can be summarized in three main points:

1. **Shared Initialization:** Tie multiple FC layers within a group of MLP modules and apply low-rank decomposition using truncated SVD, as depicted in fig. 6.
2. **Local Error Minimization:** Distill the shared initialization to minimize activation discrepancies between the original and compressed models while sparsifying the low-rank factors to optimize parameter allocation.
3. **Global Error Minimization (Optional):** Fine-tune the compressed models end-to-end to achieve optimal performance, particularly at lower compression levels.

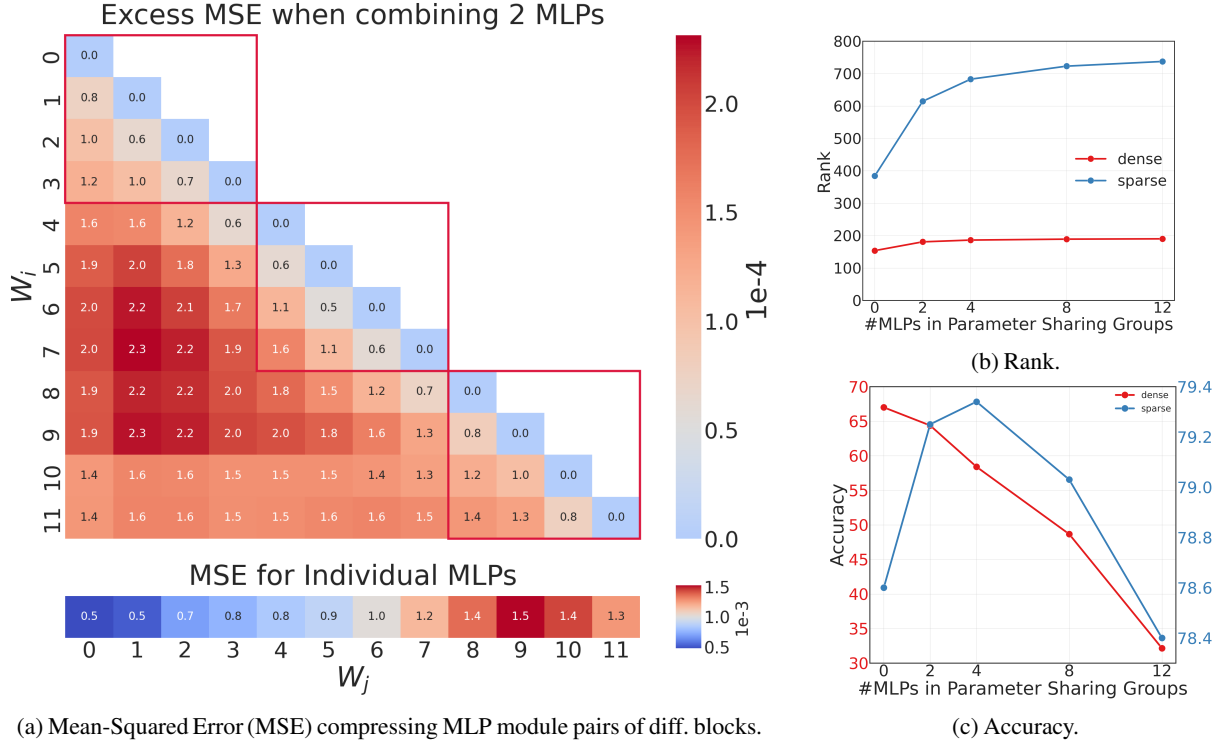


Figure 3: **Parameter Sharing Groups.** (a top) Mean squared error (MSE) increases when sharing \mathbf{U} across different MLP modules, with red squares indicating that sharing adjacent modules enhances reconstruction. (a bottom) MSE for compressing individual MLP modules, demonstrating that sharing \mathbf{U} among consecutive layers typically results in the lowest error. (b) For a fixed parameter budget, the rank of the shared basis \mathbf{U} stabilizes around four MLP modules, aligning with the optimal group size (c) for maximizing accuracy in the DeiT-B model.

Algorithm 1 outlines the key steps of FiPS, which are detailed below.

Shared Initialization. We begin by compressing the pre-trained model through parameter sharing, achieved by concatenating and decomposing multiple FC layers simultaneously.

For higher parameter budgets and sparsity levels (e.g., 26.5% and 75%, respectively, for DeiT-B), the rank of our low-rank factor \mathbf{U} can exceed the model dimension d . In such cases, we grow the matrices \mathbf{U} and \mathbf{V} similar to the approach in Net2Net (Chen et al., 2016). However, unlike Net2Net, we grow \mathbf{U} by appending zeros rather than splitting each neuron. We select the top- k neurons with the highest singular values (i.e., $k = r - d$) and multiply them by $1/\tau$, where τ is treated as a hyperparameter (i.e., neuron splitting and growing is discussed further in Appendix A.1.2).

Formally, the parameters of a group of FC layers, $\mathbf{W}_1, \mathbf{W}_2, \dots, \mathbf{W}_N$, are concatenated into a large matrix $\mathbf{W}_s = [\mathbf{W}_1; \mathbf{W}_2; \dots; \mathbf{W}_N]$, where $\mathbf{W}_i \in \mathbb{R}^{d \times p}$ ³. We

³The 2nd FC layer is transposed to match the dimensions of the 1st.

then apply truncated SVD, $\mathbf{W}_s = \mathbf{U}\Sigma\hat{\mathbf{V}}$, to obtain a low-rank approximation of the parameters, where $\mathbf{U} \in \mathbb{R}^{d \times r}$, $\Sigma \in \mathbb{R}^{r \times r}$, and $\hat{\mathbf{V}} \in \mathbb{R}^{r \times (N \cdot p)}$. The factor \mathbf{U} is shared among all layers within the group and remains dense due to its small size. Next, we multiply $\hat{\mathbf{V}}$ by the singular values to obtain the projection matrix $\mathbf{V} = \Sigma\hat{\mathbf{V}}$. Finally, the weights are reconstructed as $\mathbf{W}'_i = \mathbf{U}\mathbf{V}_i$, where each \mathbf{V}_i is a slice of \mathbf{V} corresponding to the weight matrix \mathbf{W}_i .

Local Error Minimization For the second phase of FiPS, we compute the input and output activations of the original FC layers using a calibration dataset D , described in § 4.1. We use these activations to optimize the compressed layers and minimize the L_2 -loss between the original and compressed layers' activations:

$$\underset{\mathbf{U}, \mathbf{V}_1, \dots, \mathbf{V}_N}{\operatorname{argmin}} \sum_i^N \|\mathbf{W}_i \mathbf{X}_i - \mathbf{U} \mathbf{V}_i \mathbf{X}_i\|_2^2, \quad (1)$$

where \mathbf{X}_i is the inputs to the i^{th} original FC layer. We explore several sparse training and pruning techniques to identify a sparse \mathbf{V} during this optimization: (a) *Static Sparsity*, which establishes the sparsity structure by retaining the top-

Algorithm 1 Fine-grained Parameter Sharing

Require: MLP parameters $\mathbf{W}_1, \dots, \mathbf{W}_N \in \mathbb{R}^{d \times p}$, MLP inputs \mathbf{A}_i and MLP function $\mathbf{f}(\mathbf{W}_i, \mathbf{A}_i)$, Target rank r , Learning Rate η , Steps \mathbf{T} .

- 1: $\mathbf{U}, [\mathbf{V}_1, \dots, \mathbf{V}_N] \leftarrow \text{SVD}([\mathbf{W}_1; \dots; \mathbf{W}_N], k=r)$
- 2: **for** each training iteration $t = 1$ to T **do**
- 3: $\mathbf{G}_U = 0$ {Gradient accumulator for \mathbf{U} }
- 4: **for** each block i **do**
- 5: $\mathbf{V}_i \leftarrow \text{Sparsify}(\mathbf{V}_i, t)$ {Adjust sparsity}
- 6: $L_i \leftarrow \text{MSE_loss}(\mathbf{f}(\mathbf{W}_i, \mathbf{A}_i), \mathbf{f}(\mathbf{U}\mathbf{V}_i, \mathbf{A}_i))$
- 7: $\mathbf{V}_i \leftarrow \mathbf{V}_i - \eta \nabla_{\mathbf{V}_i} L_i$
- 8: $\mathbf{G}_U \leftarrow \mathbf{G}_U + \nabla_{\mathbf{U}} L_i$
- 9: **end for**
- 10: $\mathbf{U} \leftarrow \mathbf{U} - \frac{\eta}{N} \mathbf{G}_U$
- 11: **end for**
- 12: **return** $\mathbf{U}, [\mathbf{V}_1, \dots, \mathbf{V}_N]$

magnitude connections before training (Hoeffler et al., 2021); (b) *Gradual Magnitude Pruning (GMP)* (Zhu & Gupta, 2017), which progressively increases sparsity by updating its mask every T steps, retaining the top-magnitude connections following the cubic schedule from Kurtic et al. (2023); and (c) *RigL* (Evci et al., 2021), which starts from (a) but updates the sparse connectivity every ΔT steps using gradient and magnitude information. We decided to use *GMP* for the final sparse training recipe due to its superior performance.

Although we share parameters across multiple MLP modules, gradients for error minimization can be computed one MLP module at a time. Therefore, optimization requires significantly fewer resources compared to end-to-end fine-tuning.

Global Error Minimization. In this optional stage, we fine-tune the learned parameter sharing scheme end-to-end to further improve performance. Because the factors \mathbf{V}_i are sparse, we employ the dynamic sparse training method, *RigL*, during this stage as it performs slightly better than *Static Sparsity* as discussed in § 4.1.

4 Main Results

4.1 Vision Transformers

Experimental Setup We conducted experiments using DeiT-B (12 blocks) and Swin-L (four stages with 2, 2, 18, and 2 blocks, respectively) (Touvron et al., 2021; Liu et al., 2021). A calibration dataset D consisting of 2,560 samples (20×128) from ImageNet-1k (Deng et al., 2009) was utilized. We observed that 20 epochs on this calibration set yielded near-optimal results, with longer training or larger calibration sets offering marginal gains. For both architectures, the calibration stage required less than one hour on an NVIDIA A6000 GPU. Transfer learning was evaluated on CIFAR-100, Flowers102, Oxford-III-Pets, and iNaturalist 2019 (Krizhevsky, 2009; Nilsback & Zisserman, 2008; Parkhi et al., 2012; Van Horn et al., 2018) over 100 training epochs, following the

methodology of Yu & Wu (2023). All experiments employed the *AdamW* optimizer (Loshchilov & Hutter, 2019), with optimal learning rates determined through a hyperparameter sweep over 12 logarithmically spaced values.

When applying FiPS, we targeted an average sparsity of 75% across all sparse factors, as demonstrated in Figure 4b. The mask update interval, ΔT , was set to 50 steps for both *RigL* and *GMP*. During global fine-tuning with *RigL*, the pruning ratio was set to 0.1 and reduced to 0.05 for transfer learning experiments to stabilize the sparsity pattern. Additional hyperparameter details for the optimizer and sparse training algorithms are provided in Appendix B.4.

Based on our preliminary findings (see Figure 3c), we grouped four consecutive blocks (each containing one MLP module) for DeiT-B, resulting in three parameter sharing groups. For Swin-L, parameters were shared within each 2-block stage and among three groups of six consecutive blocks in the 18-block stage.

ImageNet-1k We compared FiPS against Adaptive Atomic Feature Mimicking (AAFMM), which employs block-wise error minimization, and Global Feature Mimicking (GFM), which combines AAFMM with error minimization at the model output, requiring end-to-end tuning of the network (Yu & Wu, 2023). At a 40% parameter budget, FiPS achieved 1.36% points higher accuracy than AAFMM and surpassed the more resource-intensive GFM by 0.41% points, despite GFM requiring significantly more memory and computational resources due to end-to-end fine-tuning Table 1.

For Swin-L, similar trends were observed as shown in Table 1. Across all parameter budgets, *GMP*-based FiPS consistently outperformed alternatives like GFM, while demanding less computational and memory resources for compressing the pre-trained models.

Transfer Learning We fine-tuned our compressed models on four distinct transfer tasks, utilizing *RigL* to adapt the existing sparse factors. The models compressed with FiPS transferred significantly better, as shown in Table 2.

Latency and Memory Profiling As discussed in § 3, high levels of sparsity and parameter budgets can result in the SVD rank exceeding a model’s hidden dimension. For instance, in the case of DeiT-B, achieving 75% sparsity under parameter budget constraints exceeding 26.5% and four block groups increases the rank of the shared singular vectors beyond the original model’s embedding dimension. Efficient sparse operations and representations are crucial for minimizing the latency and memory overhead introduced by FiPS.

We present real-world benchmarks leveraging NVIDIA’s tensor core support for 2:4 sparsity (Mishra et al., 2021) on GPUs and Neural Magic’s DeepSparse Engine (Neural

Table 1: **ViT Compression Results.** Top-1 validation accuracy of DeiT-B (81.85%) (Touvron et al., 2021) and Swin-L (86.24%) (Liu et al., 2021) compressed using FiPS and AAFM/GFM across parameter budgets. The results compare layer-wise (FiPS) and global error minimization (FiPS + FT). AAFM/GFM[†] results are from Yu & Wu (2023).

Param. Budget	10%		25%		40%		50%		75%	
Method / Model	DeiT	Swin	DeiT	Swin	DeiT	Swin	DeiT	Swin	DeiT	Swin
AAFM [†]	—	—	—	—	80.33	—	81.21	85.04	—	—
GFM [†]	—	—	—	—	81.28	—	81.62	85.33	—	—
FiPS (ours)	70.04	74.04	80.64	84.78	81.69	85.69	81.83	85.99	81.82	86.21
FiPS + FT (ours)	77.26	82.13	81.31	85.16	81.55	85.68	81.54	85.99	—	—

Table 2: **Transfer Learning Results.** Comparison of Top-1 accuracy between the original DeiT-B and its compressed counterparts using GFM and FiPS across varying parameter budget constraints. Results for GFM[†] and Original[†] are sourced from Yu & Wu (2023) and Touvron et al. (2021).

Models	Original [†]	GFM [†]		FiPS+RigL FT (ours)		
Param. Budget	100%	40%	50%	25%	40%	50%
CIFAR-100	90.99	90.17	90.67	90.88	91.24	91.33
Pets	94.74	93.95	94.22	94.19	94.52	94.41
Flowers102	97.77	97.02	97.45	97.84	98.14	98.37
iNaturalist 2019	77.39	77.13	77.56	77.26	77.58	77.69

Magic, 2021) for CPU performance on fig. 7 as part of appendix B.5 and structured sparsity performance in table 5.

These results demonstrate that FiPS effectively compresses models while enhancing both memory efficiency and computational speed. For instance, with a batch size of 64, employing FiPS with 2:4 sparsity at a 22.14% parameter budget results in a $1.31\times$ speed-up on the NVIDIA A4000 and reduces maximum VRAM allocation to approximately $0.79\times$ of the original requirement during inference.

4.2 Large Language Models

Experimental Setup Four LLMs—Gemma-2 (2B, 9B) (Team et al., 2024) with 26 and 42 decoder blocks, respectively, and Llama (3.2-3B, 3.1-8B) (Grattafiori et al., 2024) with 28 and 32 decoder blocks, respectively—were calibrated using the SlimPajamas dataset (Soboleva et al., 2023). Specifically, we sampled 20 batches of 8,192 tokens, totaling 163,840 tokens, and trained for 40 epochs. The learning rate for each model was selected from 8 logarithmically spaced values, detailed in appendix B.4 along with the parameter sharing block groups. On a single NVIDIA A100 80GB GPU, calibration required less than 4 hours for the Gemma-2-2B and Llama-3.2-3B models and under 16 hours for the Gemma-2-9B and Llama-3.1-8B models.

Dataset We utilize the SlimPajama dataset (Soboleva et al., 2023), derived from the original RedPajama dataset (Weber et al., 2024) through rigorous quality filtering and deduplication, as the calibration set for FiPS. This choice is supported by findings from Bandari et al. (2024), which show that RedPajama outperforms other commonly used datasets—such as C4, OSCAR, and Pile—in calibration tasks for LLM pruning. To evaluate the generalization capabilities of the compressed LLMs, we report perplexity scores on the WikiText-2 test set (Merity et al., 2016). Unlike SlimPajama, which is used during calibration, WikiText-2 remains entirely unseen during the compression stage. This ensures an unbiased assessment of the models’ ability to generalize to new text inputs, providing a robust performance measure across different datasets and domains.

Perplexity Results Table 3 compares pure truncated SVD initialization of individual FCs with block-wise error minimization versus FiPS for compressing the MLPs of Gemma-2 and Llama-3 models at 50% and 60% parameter budgets. We report pure SVD results only for the smaller Gemma-2 and Llama-3 models to highlight their suboptimality. The results indicate that Llama models are more challenging to compress. Nevertheless, FiPS achieves strong performance relative to both SVD and its own dense baseline.

Furthermore, FiPS appears to be a viable alternative to a smaller model, as the compressed Gemma-2-9B and Llama-3.1-8B models achieve better perplexity than their smaller uncompressed counterparts, underscoring the robustness of FiPS’s parameter-sharing and sparse training framework for LLMs.

5 Ablations

In the following, we examine the importance of various components of the FiPS algorithm when compressing the DeiT-B model at the 25% parameter budget. First, we ablate the key components of our algorithm in Figure 4a:

1. **Random Initialization (RI):** Using RI instead of SVD initialization results in a 1% point drop in accuracy.

Table 3: **LLM Compression Results.** Preliminary perplexity metrics on the WikiText-2 test dataset for Gemma-2 and Llama-3 models under different parameter budgets with a context length of 2048 tokens.

Models	Original	SVD		FiPS	
		50%	60%	50%	60%
Gemma-2-2B	6.66	41.03	38.73	7.47	7.22
Gemma-2-9B	5.59	—	—	6.08	5.91
Llama-3.2-3B	6.19	45.43	41.25	9.70	7.22
Llama-3.1-8B	4.75	—	—	7.11	6.01

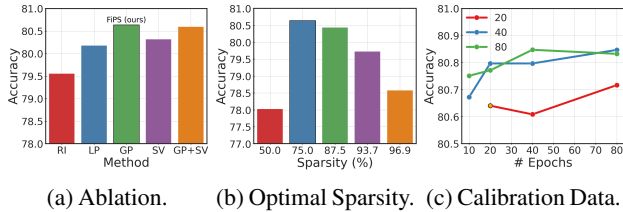


Figure 4: **DeiT-B Ablations and Sensitivity Analysis.**(a) Analysis of key components in the FiPS algorithm, including Random Initialization (RI), Local Pruning (LP), Global Pruning (GP), and Scaling Vectors (SV); (b) Impact of varying sparsity levels on performance; (c) Influence of the calibration dataset size and the number of training epochs on post-compression accuracy using a batch size of 128.

2. **Global Pruning (GP):** Using GP when sparsifying our sparse factors \mathbf{V} results in 0.4% point improvement over local pruning (LP), which enforces the same sparsity level for each factor \mathbf{V}_i .
3. **Scaling Vectors (SV):** Following Liu et al. (2024), FC weights are normalized and the magnitudes initialize the SV for neuron scaling, which enhances local pruning but is less effective than global pruning.

Consequently, the final FiPS configuration integrates GMP with GP. Next, we perform a sensitivity analysis using different sparsity levels, calibration dataset sizes, and training lengths using the DeiT-B checkpoint trained on ImageNet-1k.

Optimal Sparsity for Sparse Factors We compressed the DeiT-B model, as described in § 4.1, using sparsity levels ranging from 50% to 96.9% as shown in Figure 4b. The best performance was observed at 75% sparsity as shown in Figure 4b. While increasing sparsity to 87% yielded similar accuracy, lowering it to 50% resulted in a notable drop in performance, likely due to a significant reduction in rank.

Calibration Dataset Size and Training Length. We examine how the number of calibration batches and training epochs affects performance using a fixed batch size of 128. To ensure at least one example from each category, we begin

Table 4: **Sparsification Method and FiPS Generalization Performance.** ImageNet top-1 validation accuracy (%) of DeiT-B (81.85%) (Touvron et al., 2021) models compressed with FiPS using different sparsity methods: RigL (Evci et al., 2021) and static sparsity. Further results are presented in table 6 in appendix B.2.

Param. Budget	10%	25%	40%	50%
Dense	15.35	65.71	74.33	79.22
Static Sparsity	65.26	80.06	81.48	81.70
RigL	66.67	80.31	81.50	81.65
GMP (FiPS)	70.04	80.64	81.69	81.83

with a minimum of 10 batches and also evaluate 20, 40, and 80 batches. After filtering out any configurations that are more than 0.25% below the highest accuracy, we adopt the most efficient setting of 20 epochs over 20 batches for all reported results, as shown in Figure 4c.

Alternative Sparsity Techniques In addition to *GMP*, we evaluated *Dense* tensor decompositions (i.e., without sparsity on the \mathbf{V} factors) and other sparse training techniques, specifically *Static Sparsity* and *RigL*. The results are summarized in § 5. For DeiT-B, *RigL* consistently outperforms both *Dense* and *Static Sparsity* across parameter budgets ranging from 10% to 50%. At higher parameter budgets, all methods converge to similar accuracies approaching the original model’s performance. In the case of Swin-L, *RigL* surpasses *Dense* and *Static Sparsity* at 10% and 25% parameter budgets. However, at higher parameter budgets, *Static Sparsity* achieves slightly higher accuracies. Detailed results on Swin-L are presented in table 6 of appendix B.2.

Structured Sparsity We evaluate the generalization performance of FiPS using structured sparsity, with results presented in table 5. The methods evaluated include the Straight Through Estimator (STE), which employs top- k weight magnitude selection, projects parameters into a sparse subspace during training, and applies gradients to dense parameters through a gradual pruning schedule; the Sparse-Refined-STE (SR-STE), which mitigates the adverse effects of approximated gradients; N:M Structured RigL (NMSRigL) and N:M Structured GMP (NMSGMP) (Lee et al., 2023; Zhou et al., 2021; Lasby et al., 2024), where N:M specifies the sparsity pattern of the weight matrix (e.g., a 50% sparsity in FC matrices of size $d \times 4d$ corresponds to a 2:4 structure).

Sparsity Distribution and MSE-loss Figure 5a shows that earlier MLP layers are easier to compress, requiring fewer parameters, while later layers are more challenging, as reflected by higher reconstruction errors in Figure 3a. These later layers exhibit lower sparsity and higher weight density, with Figure 5b highlighting a strong correlation (0.922)

Table 5: **Structured Sparsity Performance.** ImageNet top-1 accuracy (%) of DeiT-B (81.85%) (Touvron et al., 2021) for structured sparsification methods at 50% sparsity, compared to Unstructured FiPS. A detailed description of each structured sparsity method is provided in § 5. Additional results can be found in table 7 in appendix B.3.

Parameter Budget	10%	25%	40%	50%
STE	42.89	73.26	78.26	79.36
SR-STE	45.31	75.53	79.71	80.68
NMSRigL	44.87	75.71	79.97	80.99
NMSGMP	52.36	76.88	80.59	81.31
FiPS (50% Sparsity)	54.00	77.56	80.94	81.63
FiPS (75% Sparsity)	70.04	80.64	81.69	81.83

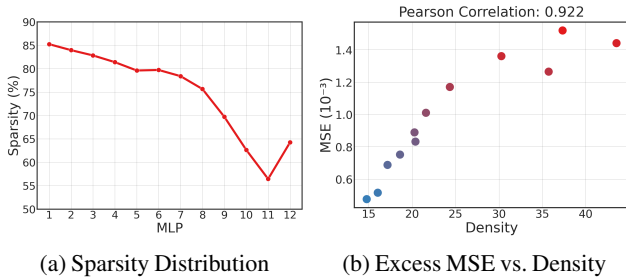


Figure 5: **DeiT-B Global Sparsity Analysis.** (a) Average sparsity at the end of the training shows that more parameters are allocated to later modules. (b) A strong correlation is observed between the MSE reported in Figure 3a and the parameter distribution identified by FiPS.

between weight density and MSE. This indicates that later layers demand more parameters to preserve performance.

Sparsity Distribution and MSE-loss Figure 5a shows that earlier MLP layers are easier to compress, requiring fewer parameters, while later layers are more challenging, as reflected by higher reconstruction errors in Figure 3a. These later layers exhibit lower sparsity and higher weight density, with Figure 5b highlighting a strong correlation (0.922) between weight density and MSE. This indicates that later layers demand more parameters to preserve performance.

6 Related Work

ViTs were introduced by Dosovitskiy et al. (2021) for image recognition, treating image patches as sequences similar to tokens in natural language processing (NLP) models. Subsequent works improved upon the original ViT design, such as Touvron et al. (2021), who enhanced data efficiency by incorporating a distillation token during training, and Liu et al. (2021), who proposed Swin Transformers. Swin

Transformers introduced a hierarchical structure and shifted windows to enable local self-attention, differentiating them from the original ViT and DeiT models.

LLMs have advanced significantly, leveraging transformer architectures to achieve state-of-the-art performance across diverse NLP tasks. These models, such as Gemma-2 and Llama-3.1 with three FC layers in their MLP modules, are typified by Yenduri et al. (2023) and demonstrate remarkable scalability and adaptability. Unlike ViTs, LLMs utilize decoder blocks optimized for autoregressive tasks, enabling sequential token prediction.

Sparsity in Neural Networks includes three main approaches: post-training pruning, sparsifying during training, and fully sparse training (Hoeffler et al., 2021). Early methods involved heuristic pruning, such as removing the smallest magnitude parameters (Thimm & Fiesler, 1995). Later approaches, like GMP (Zhu & Gupta, 2017), increased the amount of pruning, while dynamic pruning with accelerated schedulers was explored by Kurtic et al. (2023). Static sparsity uses a pre-initialized mask throughout training (Hoeffler et al., 2021), whereas dynamic methods, like RigL (Evci et al., 2021), adjust the sparsity pattern during training based on gradient information.

Tensor Decomposition techniques, such as those presented by Kolda & Bader (2009), reduce redundancy in large weight matrices using low-rank decomposition. Yu & Wu (2023) introduced AAFM for transformer models, using truncated PCA to reconstruct weights, and GFM to minimize loss between compressed and original models, similar to Knowledge Distillation (Hinton et al., 2015).

Parameter Sharing is less explored but includes works like Eban et al. (2019), which used a Sum-Product reducer to map shared parameters, and Obukhov et al. (2021), which employed TR decomposition for shared parameters in 3D tensors. Zhang et al. (2022) introduced “Weight Multiplexing,” sharing parameters between MLP modules in ViT, alongside distillation and linear projections between transformer blocks to aid model recovery.

7 Conclusion

This work introduces FiPS, demonstrating for the first time that inter-layer fine-grained parameter sharing enables substantial model compression. In § 4.1, we show that MLPs in DeiT-B and Swin-L can be compressed by up to 75% while maintaining accuracy within 1% pt. of the original, and those in Gemma-2 and Llama-3 models by up to 50% with negligible perplexity drop. While this study focuses on MLP modules in ViT backbones and LLMs, similar gains are likely for multi-head attention projections. Further improvements may be possible by quantizing the current full-precision bases, which we leave for future work.

Impact Statement

This paper advances Machine Learning by introducing **Fine-grained Parameter Sharing (FiPS)**, a model compression method that improves the efficiency of Vision Transformers (ViTs) and Large Language Models (LLMs). By leveraging parameter sharing, tensor decomposition, and sparsity, FiPS reduces computational and memory costs, enhancing AI accessibility on resource-constrained devices.

While model compression promotes efficiency and sustainability, it may also enable broader AI deployment in sensitive domains with ethical concerns such as bias, misinformation, and privacy. This work does not introduce new risks beyond those inherent in deep learning, but we encourage responsible deployment and ethical considerations in practice.

Author Contributions

Cem Üyük led the project, proposed and executed the experimental plan, facilitated the team meetings, developed the software architecture, implemented static sparse training algorithm and provided code review for the sparse training algorithms, wrote the first draft of the paper. Mike Lasby implemented sparse training algorithms, assisted the software architecture development, handled distributed training integration, performed code reviews, and assisted with writing and proofreading the paper. Mohamed Yassin assisted with coding and running inference experiments. Utku Evci proposed the project and its central idea, contributed to the research plan and direction, advised Cem, reviewed the code, helped substantially with the writing, and created some of the plots. Yani Ioannou helped with the research direction, contributed to the paper’s motivation, helped with the writing, provided compute resources, and supervised the work by members of the Calgary ML Lab at the University of Calgary, including Cem Üyük (Visiting Student Researcher), Mike Lasby (PhD Student), and Mohamed Yassin (Research Assistant).

Acknowledgments

We acknowledge the support of Alberta Innovates (ALLRP-577350-22, ALLRP-222301502), the Natural Sciences and Engineering Research Council of Canada (RGPIN-2022-03120, DGEER-2022-00358), and Defence Research and Development Canada (DGDND-2022-03120). This research was enabled in part by support provided by the Digital Research Alliance of Canada (alliancecan.ca) and Google Cloud. We also acknowledge Erik Schultheis’ very helpful feedback with regard to custom kernel design.

References

Bandari, A., Yin, L., Hsieh, C.-Y., Jaiswal, A. K., Chen, T., Shen, L., Krishna, R., and Liu, S. Is c4 dataset optimal for pruning? an investigation of calibration data for llm pruning, 2024. URL

<https://arxiv.org/abs/2410.07461>.

Chen, T., Goodfellow, I., and Shlens, J. Net2net: Accelerating learning via knowledge transfer, 2016. URL <https://arxiv.org/abs/1511.05641>.

Cheng, Y., Wang, D., Zhou, P., and Zhang, T. A survey of model compression and acceleration for deep neural networks, 2020. URL <https://arxiv.org/abs/1710.09282>.

Deng, J., Dong, W., Socher, R., Li, L.-J., Li, K., and Fei-Fei, L. Imagenet: A large-scale hierarchical image database. In *2009 IEEE Conference on Computer Vision and Pattern Recognition*, pp. 248–255. IEEE, 2009.

Dosovitskiy, A., Beyer, L., Kolesnikov, A., Weissenborn, D., Zhai, X., Unterthiner, T., Dehghani, M., Minderer, M., Heigold, G., Gelly, S., Uszkoreit, J., and Houlsby, N. An image is worth 16x16 words: Transformers for image recognition at scale, 2021. URL <https://arxiv.org/abs/2010.11929>.

Eban, E., Movshovitz-Attias, Y., Wu, H., Sandler, M., Poon, A., Idelbayev, Y., and Carreira-Perpinan, M. A. Structured multi-hashing for model compression, 2019. URL <https://arxiv.org/abs/1911.11177>.

Evci, U., Gale, T., Menick, J., Castro, P. S., and Elsen, E. Rigging the lottery: Making all tickets winners, 2021. URL <https://arxiv.org/abs/1911.11134>.

Evci, U., van Merriënboer, B., Unterthiner, T., Vladymyrov, M., and Pedregosa, F. Gradmax: Growing neural networks using gradient information, 2022. URL <https://arxiv.org/abs/2201.05125>.

Grattafiori, A., Dubey, A., Jauhri, A., Pandey, A., Kadian, A., Al-Dahle, A., Letman, A., Mathur, A., Schelten, A., Vaughan, A., Yang, A., Fan, A., Goyal, A., Hartshorn, A., Yang, A., Mitra, A., Sravankumar, A., Korenev, A., Hinsvark, A., Rao, A., Zhang, A., Rodriguez, A., Gregerson, A., Spataru, A., Roziere, B., Biron, B., Tang, B., Chern, B., Caucheteux, C., Nayak, C., Bi, C., Marra, C., McConnell, C., Keller, C., Touret, C., Wu, C., Wong, C., Ferrer, C. C., Nikolaidis, C., Allonsius, D., Song, D., Pintz, D., Livshits, D., Wyatt, D., Esiobu, D., Choudhary, D., Mahajan, D., Garcia-Olano, D., Perino, D., Hupkes, D., Lomakin, E., AlBadawy, E., Lobanova, E., Dinan, E., Smith, E. M., Radenovic, F., Guzmán, F., Zhang, F., Synnaeve, G., Lee, G., Anderson, G. L., Thattai, G., Nail, G., Mialon, G., Pang, G., Cucurell, G., Nguyen, H., Korevaar, H., Xu, H., Touvron, H., Zarov, I., Ibarra, I. A., Kloumann, I., Misra, I., Evtimov, I., Zhang, J., Copet, J., Lee, J., Geffert, J., Vranes, J., Park, J., Mahadeokar, J., Shah, J., van der Linde, J., Billoock, J., Hong, J., Lee, J., Fu, J., Chi, J., Huang, J., Liu, J., Wang, J., Yu, J., Bitton,

- J., Spisak, J., Park, J., Rocca, J., Johnstun, J., Saxe, J., Jia, J., Alwala, K. V., Prasad, K., Upasani, K., Plawiak, K., Li, K., Heafield, K., Stone, K., El-Arini, K., Iyer, K., Malik, K., Chiu, K., Bhalla, K., Lakhotia, K., Rantala-Yearly, L., van der Maaten, L., Chen, L., Tan, L., Jenkins, L., Martin, L., Madaan, L., Malo, L., Blecher, L., Landzaat, L., de Oliveira, L., Muzzi, M., Pasupuleti, M., Singh, M., Paluri, M., Kardas, M., Tsimpoukelli, M., Oldham, M., Rita, M., Pavlova, M., Kambadur, M., Lewis, M., Si, M., Singh, M. K., Hassan, M., Goyal, N., Torabi, N., Bashlykov, N., Bogoychev, N., Chatterji, N., Zhang, N., Duchenne, O., Çelebi, O., Alrassy, P., Zhang, P., Li, P., Vasic, P., Weng, P., Bhargava, P., Dubal, P., Krishnan, P., Koura, P. S., Xu, P., He, Q., Dong, Q., Srinivasan, R., Ganapathy, R., Calderer, R., Cabral, R. S., Stojnic, R., Raileanu, R., Maheswari, R., Girdhar, R., Patel, R., Sauvestre, R., Polidoro, R., Sumbaly, R., Taylor, R., Silva, R., Hou, R., Wang, R., Hosseini, S., Chennabasappa, S., Singh, S., Bell, S., Kim, S. S., Edunov, S., Nie, S., Narang, S., Raparthy, S., Shen, S., Wan, S., Bhosale, S., Zhang, S., Vandenhende, S., Batra, S., Whitman, S., Sootla, S., Collot, S., Gururangan, S., Borodinsky, S., Herman, T., Fowler, T., Sheasha, T., Georgiou, T., Scialom, T., Speckbacher, T., Mihaylov, T., Xiao, T., Karn, U., Goswami, V., Gupta, V., Ramanathan, V., Kerkez, V., Gonguet, V., Do, V., Vogeti, V., Albiero, V., Petrovic, V., Chu, W., Xiong, W., Fu, W., Meers, W., Martinet, X., Wang, X., Wang, X., Tan, X. E., Xia, X., Xie, X., Jia, X., Wang, X., Goldschlag, Y., Gaur, Y., Babaei, Y., Wen, Y., Song, Y., Zhang, Y., Li, Y., Mao, Y., Coudert, Z. D., Yan, Z., Chen, Z., Papakipos, Z., Singh, A., Srivastava, A., Jain, A., Kelsey, A., Shajnfeld, A., Gangidi, A., Victoria, A., Goldstand, A., Menon, A., Sharma, A., Boesenberg, A., Baevski, A., Feinstein, A., Kallet, A., Sangani, A., Teo, A., Yunus, A., Lupu, A., Alvarado, A., Caples, A., Gu, A., Ho, A., Poulton, A., Ryan, A., Ramchandani, A., Dong, A., Franco, A., Goyal, A., Saraf, A., Chowdhury, A., Gabriel, A., Bharambe, A., Eisenman, A., Yazdan, A., James, B., Maurer, B., Leonhardi, B., Huang, B., Loyd, B., Paola, B. D., Paranjape, B., Liu, B., Wu, B., Ni, B., Hancock, B., Wasti, B., Spence, B., Stojkovic, B., Gamido, B., Montalvo, B., Parker, C., Burton, C., Mejia, C., Liu, C., Wang, C., Kim, C., Zhou, C., Hu, C., Chu, C.-H., Cai, C., Tindal, C., Feichtenhofer, C., Gao, C., Civin, D., Beaty, D., Kreymer, D., Li, D., Adkins, D., Xu, D., Testuggine, D., David, D., Parikh, D., Liskovich, D., Foss, D., Wang, D., Le, D., Holland, D., Dowling, E., Jamil, E., Montgomery, E., Presani, E., Hahn, E., Wood, E., Le, E.-T., Brinkman, E., Arcaute, E., Dunbar, E., Smothers, E., Sun, F., Kreuk, F., Tian, F., Kokkinos, F., Ozgenel, F., Caggioni, F., Kanayet, F., Seide, F., Florez, G. M., Schwarz, G., Badeer, G., Swee, G., Halpern, G., Herman, G., Sizov, G., Guangyi, Zhang, Lakshminarayanan, G., Inan, H., Shojanazeri, H., Zou, H., Wang, H., Zha, H., Habeeb, H., Rudolph, H., Suk, H., Aspegren, H., Goldman, H., Zhan, H., Damla, I., Molybog, I., Tufanov, I., Leontiadis, I., Veliche, I.-E., Gat, I., Weissman, J., Geboski, J., Kohli, J., Lam, J., Asher, J., Gaya, J.-B., Marcus, J., Tang, J., Chan, J., Zhen, J., Reizenstein, J., Teboul, J., Zhong, J., Jin, J., Yang, J., Cummings, J., Carvill, J., Shepard, J., McPhie, J., Torres, J., Ginsburg, J., Wang, J., Wu, K., U, K. H., Saxena, K., Khandelwal, K., Zand, K., Matosich, K., Veeraraghavan, K., Michelena, K., Li, K., Jagadeesh, K., Huang, K., Chawla, K., Huang, K., Chen, L., Garg, L., A, L., Silva, L., Bell, L., Zhang, L., Guo, L., Yu, L., Moshkovich, L., Wehrstedt, L., Khabsa, M., Avalani, M., Bhatt, M., Mankus, M., Hasson, M., Lennie, M., Reso, M., Groshev, M., Naumov, M., Lathi, M., Keneally, M., Liu, M., Seltzer, M. L., Valko, M., Restrepo, M., Patel, M., Vyatskov, M., Samvelyan, M., Clark, M., Macey, M., Wang, M., Hermoso, M. J., Metanat, M., Rastegari, M., Bansal, M., Santhanam, N., Parks, N., White, N., Bawa, N., Singhal, N., Egebo, N., Usunier, N., Mehta, N., Laptev, N. P., Dong, N., Cheng, N., Chernoguz, O., Hart, O., Salpekar, O., Kalinli, O., Kent, P., Parekh, P., Saab, P., Balaji, P., Rittner, P., Bontrager, P., Roux, P., Dollar, P., Zvyagina, P., Ratanchandani, P., Yuvraj, P., Liang, Q., Alao, R., Rodriguez, R., Ayub, R., Murthy, R., Nayani, R., Mitra, R., Parthasarathy, R., Li, R., Hogan, R., Battey, R., Wang, R., Howes, R., Rinott, R., Mehta, S., Siby, S., Bondu, S. J., Datta, S., Chugh, S., Hunt, S., Dhillon, S., Sidorov, S., Pan, S., Mahajan, S., Verma, S., Yamamoto, S., Ramaswamy, S., Lindsay, S., Lindsay, S., Feng, S., Lin, S., Zha, S. C., Patil, S., Shankar, S., Zhang, S., Zhang, S., Wang, S., Agarwal, S., Sajuyigbe, S., Chintala, S., Max, S., Chen, S., Kehoe, S., Satterfield, S., Govindaprasad, S., Gupta, S., Deng, S., Cho, S., Virk, S., Subramanian, S., Choudhury, S., Goldman, S., Remez, T., Glaser, T., Best, T., Koehler, T., Robinson, T., Li, T., Zhang, T., Matthews, T., Chou, T., Shaked, T., Vontimitta, V., Ajayi, V., Montanez, V., Mohan, V., Kumar, V. S., Mangla, V., Ionescu, V., Poenaru, V., Mihailescu, V. T., Ivanov, V., Li, W., Wang, W., Jiang, W., Bouaziz, W., Constable, W., Tang, X., Wu, X., Wang, X., Wu, X., Gao, X., Kleinman, Y., Chen, Y., Hu, Y., Jia, Y., Qi, Y., Li, Y., Zhang, Y., Zhang, Y., Adi, Y., Nam, Y., Yu, Wang, Zhao, Y., Hao, Y., Qian, Y., Li, Y., He, Y., Rait, Z., DeVito, Z., Rosnbrick, Z., Wen, Z., Yang, Z., Zhao, Z., and Ma, Z. The llama 3 herd of models, 2024. URL <https://arxiv.org/abs/2407.21783>.
- He, K., Zhang, X., Ren, S., and Sun, J. Delving deep into rectifiers: Surpassing human-level performance on imagenet classification, 2015. URL <https://arxiv.org/abs/1502.01852>.
- Hinton, G., Vinyals, O., and Dean, J. Distilling the knowledge in a neural network. In *Advances in Neural Information Processing Systems (NIPS) Deep Learning and Representation Learning Workshop*, 2015.
- Hoefer, T., Alistarh, D., Ben-Nun, T., Dryden, N., and Peste,

- A. Sparsity in deep learning: Pruning and growth for efficient inference and training in neural networks, 2021. URL <https://arxiv.org/abs/2102.00554>.
- Kolda, T. G. and Bader, B. W. Tensor decompositions and applications. *SIAM Rev.*, 51:455–500, 2009. URL <https://api.semanticscholar.org/CorpusID:16074195>.
- Krizhevsky, A. Learning multiple layers of features from tiny images. Technical Report TR-2009, University of Toronto, 2009.
- Kurtic, E., Hoeffler, T., and Alistarh, D. How to prune your language model: Recovering accuracy on the "sparsity may cry" benchmark, 2023. URL <https://arxiv.org/abs/2312.13547>.
- Lan, Z., Chen, M., Goodman, S., Gimpel, K., Sharma, P., and Soricut, R. Albert: A lite bert for self-supervised learning of language representations, 2020. URL <https://arxiv.org/abs/1909.11942>.
- Lasby, M., Golubeva, A., Evci, U., Nica, M., and Ioannou, Y. Dynamic sparse training with structured sparsity. In *International Conference on Learning Representations (ICLR)*, 2024.
- Lee, J., Park, W., Mitchell, N., Pilault, J., Obando-Ceron, J., Kim, H.-B., Lee, N., Frantar, E., Long, Y., Yazdanbakhsh, A., Agrawal, S., Subramanian, S., Wang, X., Kao, S.-C., Zhang, X., Gale, T., Bik, A., Han, W., Ferev, M., and Evci, U. Jaxpruner: A concise library for sparsity research, 04 2023.
- Lin, Y., Wang, M., Zhang, Z., Wang, X., Xiao, T., and Zhu, J. Understanding parameter sharing in transformers, 2023. URL <https://arxiv.org/abs/2306.09380>.
- Liu, S.-Y., Wang, C.-Y., Yin, H., Molchanov, P., Wang, Y.-C. F., Cheng, K.-T., and Chen, M.-H. Dora: Weight-decomposed low-rank adaptation, 2024. URL <https://arxiv.org/abs/2402.09353>.
- Liu, Z., Lin, Y., Cao, Y., Hu, H., Wei, Y., Zhang, Z., Lin, S., and Guo, B. Swin transformer: Hierarchical vision transformer using shifted windows, 2021. URL <https://arxiv.org/abs/2103.14030>.
- Loshchilov, I. and Hutter, F. Decoupled weight decay regularization, 2019. URL <https://arxiv.org/abs/1711.05101>.
- Merity, S., Xiong, C., Bradbury, J., and Socher, R. Pointer sentinel mixture models, 2016. URL <https://arxiv.org/abs/1609.07843>.
- Mishra, A., Latorre, J. A., Pool, J., Stosic, D., Stosic, D., Venkatesh, G., Yu, C., and Micikevicius, P. Accelerating Sparse Deep Neural Networks, April 2021. URL <http://arxiv.org/abs/2104.08378>. arXiv:2104.08378 [cs].
- Neural Magic. DeepSparse engine: Sparsity-aware deep learning inference runtime for CPUs, 2021. URL <https://github.com/neuralmagic/deepsparse>.
- Nilsback, M.-E. and Zisserman, A. Automated flower classification over a large number of classes. In *Proceedings of the Indian Conference on Computer Vision, Graphics and Image Processing*, pp. 722–729. IEEE, 2008.
- Obukhov, A., Rakhuba, M., Georgoulis, S., Kanakis, M., Dai, D., and Gool, L. V. T-basis: a compact representation for neural networks, 2021. URL <https://arxiv.org/abs/2007.06631>.
- Parkhi, O. M., Vedaldi, A., Zisserman, A., and Jawahar, C. V. Cats and dogs. IEEE Conference on Computer Vision and Pattern Recognition, 2012. The Oxford-IIIT Pet Dataset.
- Soboleva, D., Al-Khateeb, F., Myers, R., Steeves, J. R., Hestness, J., and Dey, N. SlimPajama: A 627B token cleaned and deduplicated version of RedPajama. <https://www.cerebras.net/blog/slimpajama-a-627b-token-cleaned-and-deduplicated-version-of-RedPajama>. 6 2023. URL <https://huggingface.co/datasets/cerebras/SlimPajama-627B>.
- Takase, S. and Kiyono, S. Lessons on parameter sharing across layers in transformers, 2023. URL <https://arxiv.org/abs/2104.06022>.
- Team, G., Riviere, M., Pathak, S., Sessa, P. G., Hardin, C., Bhupatiraju, S., Hussenot, L., Mesnard, T., Shahriari, B., Ramé, A., Ferret, J., Liu, P., Tafti, P., Friesen, A., Casbon, M., Ramos, S., Kumar, R., Lan, C. L., Jerome, S., Tsitsulin, A., Vieillard, N., Stanczyk, P., Girgin, S., Momchev, N., Hoffman, M., Thakoor, S., Grill, J.-B., Neyshabur, B., Bachem, O., Walton, A., Severyn, A., Parrish, A., Ahmad, A., Hutchison, A., Abdagic, A., Carl, A., Shen, A., Brock, A., Coenen, A., Laforge, A., Paterson, A., Bastian, B., Piot, B., Wu, B., Royal, B., Chen, C., Kumar, C., Perry, C., Welty, C., Choquette-Choo, C. A., Sinopalnikov, D., Weinberger, D., Vijaykumar, D., Rogozińska, D., Herbison, D., Bandy, E., Wang, E., Noland, E., Moreira, E., Senter, E., Eltyshiev, E., Visin, F., Rasskin, G., Wei, G., Cameron, G., Martins, G., Hashemi, H., Klimczak-Plucińska, H., Batra, H., Dhand, H., Nardini, I., Mein, J., Zhou, J., Svensson, J., Stanway, J., Chan, J., Zhou, J. P., Carrasqueira, J., Iljazi,

- J., Becker, J., Fernandez, J., van Amersfoort, J., Gordon, J., Lipschultz, J., Newlan, J., yeong Ji, J., Mohamed, K., Badola, K., Black, K., Millican, K., McDonell, K., Nguyen, K., Sodhia, K., Greene, K., Sjoesund, L. L., Usui, L., Sifre, L., Heuermann, L., Lago, L., McNealus, L., Soares, L. B., Kilpatrick, L., Dixon, L., Martins, L., Reid, M., Singh, M., Iverson, M., Görner, M., Velloso, M., Wirth, M., Davidow, M., Miller, M., Rahtz, M., Watson, M., Risdal, M., Kazemi, M., Moynihan, M., Zhang, M., Kahng, M., Park, M., Rahman, M., Khatwani, M., Dao, N., Bardoliwalla, N., Devanathan, N., Dumai, N., Chauhan, N., Wahltinez, O., Botarda, P., Barnes, P., Barham, P., Michel, P., Jin, P., Georgiev, P., Culliton, P., Kuppala, P., Comanescu, R., Merhej, R., Jana, R., Rokni, R. A., Agarwal, R., Mullins, R., Saadat, S., Carthy, S. M., Cogan, S., Perrin, S., Arnold, S. M. R., Krause, S., Dai, S., Garg, S., Sheth, S., Ronstrom, S., Chan, S., Jordan, T., Yu, T., Eccles, T., Hennigan, T., Kocisky, T., Doshi, T., Jain, V., Yadav, V., Meshram, V., Dharmadhikari, V., Barkley, W., Wei, W., Ye, W., Han, W., Kwon, W., Xu, X., Shen, Z., Gong, Z., Wei, Z., Cotruta, V., Kirk, P., Rao, A., Giang, M., Peran, L., Warkentin, T., Collins, E., Barral, J., Ghahramani, Z., Hadsell, R., Sculley, D., Banks, J., Dragan, A., Petrov, S., Vinyals, O., Dean, J., Hassabis, D., Kavukcuoglu, K., Farabet, C., Buchatskaya, E., Borgeaud, S., Fiedel, N., Joulin, A., Kenealy, K., Dadashi, R., and Andreev, A. Gemma 2: Improving open language models at a practical size, 2024. URL <https://arxiv.org/abs/2408.00118>.
- Thimm, G. and Fiesler, E. Evaluating pruning methods. In *International Symposium on Artificial Neural Networks*, 1995. URL <https://api.semanticscholar.org/CorpusID:11075297>.
- Touvron, H., Cord, M., Douze, M., Massa, F., Sablayrolles, A., and Jégou, H. Training data-efficient image transformers & distillation through attention, 2021. URL <https://arxiv.org/abs/2012.12877>.
- Van Horn, G., Mac Aodha, O., Marquis, T., Su, S., Haghighi, M., Baldrige, J., Maji, S., and Perona, P. The inaturalist species classification and detection dataset. In *Proceedings of the IEEE Conference on Computer Vision and Pattern Recognition (CVPR)*, pp. 8769–8778. IEEE, 2018.
- Weber, M., Fu, D., Anthony, Q., Oren, Y., Adams, S., Alexandrov, A., Lyu, X., Nguyen, H., Yao, X., Adams, V., Athiwaratkun, B., Chalamala, R., Chen, K., Ryabinin, M., Dao, T., Liang, P., Ré, C., Rish, I., and Zhang, C. Redpajama: an open dataset for training large language models, 2024. URL <https://arxiv.org/abs/2411.12372>.
- Yenduri, G., M, R., G, C. S., Y, S., Srivastava, G., Maddikunta, P. K. R., G, D. R., Jhaveri, R. H., B, P., Wang, W., Vasilakos, A. V., and Gadekallu, T. R. Generative pre-trained transformer: A comprehensive review on enabling technologies, potential applications, emerging challenges, and future directions, 2023. URL <https://arxiv.org/abs/2305.10435>.
- Yu, H. and Wu, J. Compressing transformers. In *Proceedings of the Thirty-Seventh AAAI Conference on Artificial Intelligence and Thirty-Fifth Conference on Innovative Applications of Artificial Intelligence and Thirteenth Symposium on Educational Advances in Artificial Intelligence*, AAAI’23/IAAI’23/EAAI’23. AAAI Press, 2023. ISBN 978-1-57735-880-0. doi: 10.1609/aaai.v37i9.26304. URL <https://doi.org/10.1609/aaai.v37i9.26304>.
- Zhang, J., Peng, H., Wu, K., Liu, M., Xiao, B., Fu, J., and Yuan, L. Minivit: Compressing vision transformers with weight multiplexing, 2022. URL <https://arxiv.org/abs/2204.07154>.
- Zhou, A., Ma, Y., Zhu, J., Liu, J., Zhang, Z., Yuan, K., Sun, W., and Li, H. Learning n:m fine-grained structured sparse neural networks from scratch, 2021. URL <https://arxiv.org/abs/2102.04010>.
- Zhu, M. and Gupta, S. To prune, or not to prune: exploring the efficacy of pruning for model compression, 2017. URL <https://arxiv.org/abs/1710.01878>.

A Appendix

A.1 Method

The overall method is depicted in fig. 6, and further details are explained below.

A.1.1 MLP CONCATENATION STRATEGIES

In reference to § 2.2, below is a detailed account of MLP concatenation setups. Considering two MLPs, therefore, 4 FC layers and assuming each weight matrix $\mathbf{W}_{ij} \in \mathbb{R}^{d \times p}$ (where $p = 4d$ and $i, j \in \{1, 2\}$), we identify four distinct methods for concatenating the FC weights:

I. All weights are combined along the longer dimension, resulting in:

$$\mathbf{W} = [\mathbf{W}_1; \mathbf{W}_2; \mathbf{W}_3; \mathbf{W}_4] \in \mathbb{R}^{d \times 16d}.$$

II. The FC1 and FC2 weights from each MLP are concatenated along the longer axis, followed by concatenation along the shorter axis. Specifically, we have:

$$\mathbf{W}_1 = [\mathbf{W}_{11}; \mathbf{W}_{12}] \in \mathbb{R}^{d \times 8d} \quad \text{and} \quad \mathbf{W}_2 = [\mathbf{W}_{21}; \mathbf{W}_{22}] \in \mathbb{R}^{d \times 8d},$$

leading to:

$$\mathbf{W} = [\mathbf{W}_1; \mathbf{W}_2] \in \mathbb{R}^{2d \times 8d}.$$

III. The FC1 weights from both MLPs are concatenated along the longer axis, followed by concatenating the FC2 weights similarly. This results in:

$$\mathbf{W}_1 = [\mathbf{W}_{11}; \mathbf{W}_{21}] \in \mathbb{R}^{d \times 8d} \quad \text{and} \quad \mathbf{W}_2 = [\mathbf{W}_{12}; \mathbf{W}_{22}] \in \mathbb{R}^{d \times 8d},$$

yielding:

$$\mathbf{W} = [\mathbf{W}_1; \mathbf{W}_2] \in \mathbb{R}^{2d \times 8d}.$$

IV. Finally, all weights are concatenated along the shorter axis:

$$\mathbf{W} = [\mathbf{W}_1; \mathbf{W}_2; \mathbf{W}_3; \mathbf{W}_4] \in \mathbb{R}^{4d \times 4d}.$$

These configurations are explored empirically in Figure 2c and discussed in full in § 2.2.

A.1.2 GROWING NEURONS IN SHARED BASES AND SPARSE FACTORS

As discussed in § 3, high parameter budgets and sparsity levels (e.g., 26.5% parameter budget, 75% sparsity and groups of four blocks in DeiT-B) often result in the rank r exceeding the model dimension d . Since SVD yields only d initialization directions, we investigate three methods to initialize the remaining $k = r - d$ dimensions: 1. **Random Growth**: Initialize new neurons in \mathbf{U} to zero and in \mathbf{V} randomly using He et al. (2015); 2. **Neuron Splitting**: Duplicate the top k neurons of \mathbf{U} and halve the top k neurons of \mathbf{V} , following Chen et al. (2016); 3. **Hybrid Initialization**: Initialize new neurons in \mathbf{U} to zero and derive those in \mathbf{V} from the top k neurons, normalized by τ . This method minimizes the immediate impact of new neurons in \mathbf{V} , allowing their gradual reactivation, as proposed by Evci et al. (2022). After performing a hyperparameter sweep for τ , hybrid initialization outperformed the alternatives, achieving 1% and 2% higher accuracy than methods (1) and (2), respectively.

B Results and Ablation

B.1 Model Links

- DeiT-B (Touvron et al., 2021): huggingface.co/facebook/deit-base-patch16-224
- Swin-L (Liu et al., 2021): huggingface.co/microsoft/swin-large-patch4-window7-224
- Gemma-2-2B (Team et al., 2024): huggingface.co/google/gemma-2-2b

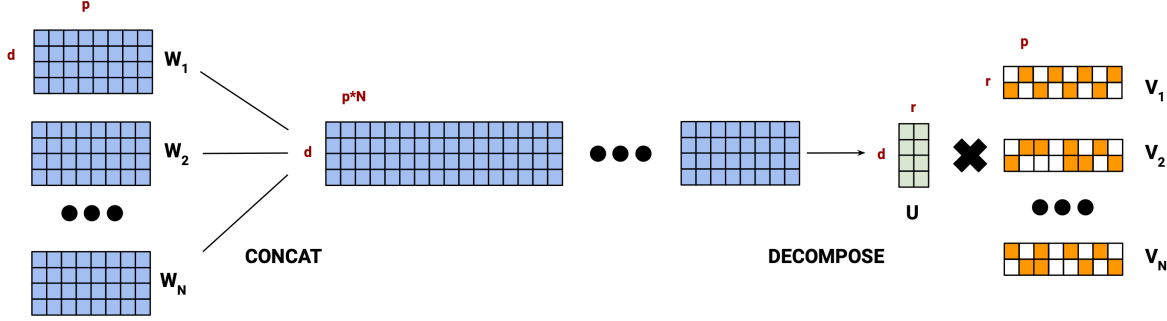


Figure 6: **Parameter Sharing Through Sparse Tensor Decomposition.** A group of FC layers are concatenated along the larger dimension, p , and decomposed into two matrices: a shared basis, U , and a sparse projection matrix, which is then sliced up respectively for each layer.

Table 6: **Sparsification Method and FiPS Generalization Performance.** ImageNet top-1 validation accuracy (%) of DeiT-B (81.85%) (Touvron et al., 2021) and Swin-L (86.24%) (Liu et al., 2021) models compressed with FiPS using different sparsity methods: RigL (Evci et al., 2021) and static sparsity.

Param. Budget	10%		25%		40%		50%		75%	
Method / Model	DeiT	Swin	DeiT	Swin	DeiT	Swin	DeiT	Swin	DeiT	Swin
Dense	15.35	3.61	65.71	60.31	74.33	80.61	79.22	83.59	81.36	85.64
Static Sparsity	65.26	65.6	80.06	84.37	81.48	85.69	81.70	85.98	81.86	86.23
RigL	66.67	70.96	80.31	84.57	81.50	85.59	81.65	85.91	81.82	86.20
GMP (FiPS)	70.04	74.04	80.64	84.78	81.69	85.69	81.83	85.99	81.82	86.21

- Gemma-2-9B (Team et al., 2024): huggingface.co/google/gemma-2-9b
- Llama-3.2-3B (Grattafiori et al., 2024): huggingface.co/meta-Llama/Llama-3.2-3B
- Llama-3.1-8B (Grattafiori et al., 2024): huggingface.co/meta-Llama/Llama-3.1-8B

B.2 Different Sparsification Methods

The full results for various sparsification methods applied to DeiT-B and Swin-L models are presented in table 6.

B.3 Structured Sparsity

As stated in § 5, table 7 showcases the full extent of structured sparsity results across varying parameter budgets.

B.4 Hyper-parameters

Block Groups As described in § 4.1, we grouped four consecutive blocks (each containing one MLP module) for DeiT-B, resulting in three parameter-sharing groups. For Swin-L, parameters were shared within each 2-block stage and across three groups of six consecutive blocks within the 18-block stage.

For Gemma-2-2B, the first two blocks were grouped together, followed by groups of six blocks each until the 26th block. Similarly, for Gemma-2-9B, blocks were divided into six groups, extending up to the 42nd block.

For Llama-3.2-3B, each group contained seven blocks, forming a total of four groups. Finally, Llama-3.1-8B was divided into four parameter-sharing groups, each containing eight blocks.

Optimizer

Table 7: **Structured Sparsity Performance.** ImageNet top-1 validation accuracy (%) of DeiT-B (81.85%) (Touvron et al., 2021) for various structured sparsification methods at 50% and 75% sparsity, compared to Unstructured FiPS. Methods include STE, Sparse-Refined STE, N:M Structured RigL (NMSRigL), and N:M Structured GMP (NMSGMP) at 50% sparsity, corresponding to 2:4 structures (Lee et al., 2023; Zhou et al., 2021; Lasby et al., 2024).

Parameter Budget	10%	25%	40%	50%	75%
STE	42.89	73.26	78.26	79.36	78.89
SR-STE	45.31	75.53	79.71	80.68	81.24
NMSRigL	44.87	75.71	79.97	80.99	81.40
NMSGMP	52.36	76.88	80.59	81.31	81.51
FiPS (50% Sparsity)	54.00	77.56	80.94	81.63	81.77
FiPS (75% Sparsity)	70.04	80.64	81.69	81.83	81.82

ViT Compression. To minimize local error, we employ a logarithmic grid for hyperparameter tuning. The learning rates for Dense, Static Sparsity, GMP, and RigL are set as follows for both DeiT-B and Swin-L:

1. Dense: 1.25×10^{-4} ,
2. Static Sparsity: 2.5×10^{-4} ,
3. GMP: 1×10^{-3} ,
4. RigL: 1×10^{-3} .

ViT Transfer Learning. We use a linear grid, as some hyperparameters are derived from the codebase of DeiT. The optimal learning rates for FiPS are:

1. CIFAR-100: 2.5×10^{-5} ;
2. Flowers102: 1×10^{-4} ;
3. Oxford-III-Pets: 7.5×10^{-6} ;
4. iNaturalist 2019: 1×10^{-4} .

LLMs Eight logarithmically spaced values were swept. The final values for FiPS are presented below:

1. Gemma-2-2B: 3.125×10^{-5} ,
2. Gemma-2-9B: 3.125×10^{-5} ,
3. Llama-3.2-3B: 4.0×10^{-6} ,
4. Llama-3.1-8B: 8.0×10^{-6} .

Sparsifier

Global Mask Pruning (GMP) GMP begins with an initial sparsity level of 25%. During the training process, the sparsity is gradually increased to 50% at the 25% training mark and ultimately reaches 75% sparsity by the end of the training. The ΔT of 50 is used for update steps.

RigL RigL employs an initialization phase that combines pruning with a growth ratio of 0.1 for block-wise error minimization and a growth ratio of 0.05 for transfer learning tasks with ΔT of 50 for growth and pruning ratio. This more conservative growth ratio in transfer learning helps preserve the mask obtained during the error minimization, ensuring that important masks learned during the initial training are not lost.

B.5 Latency and Memory Profiling

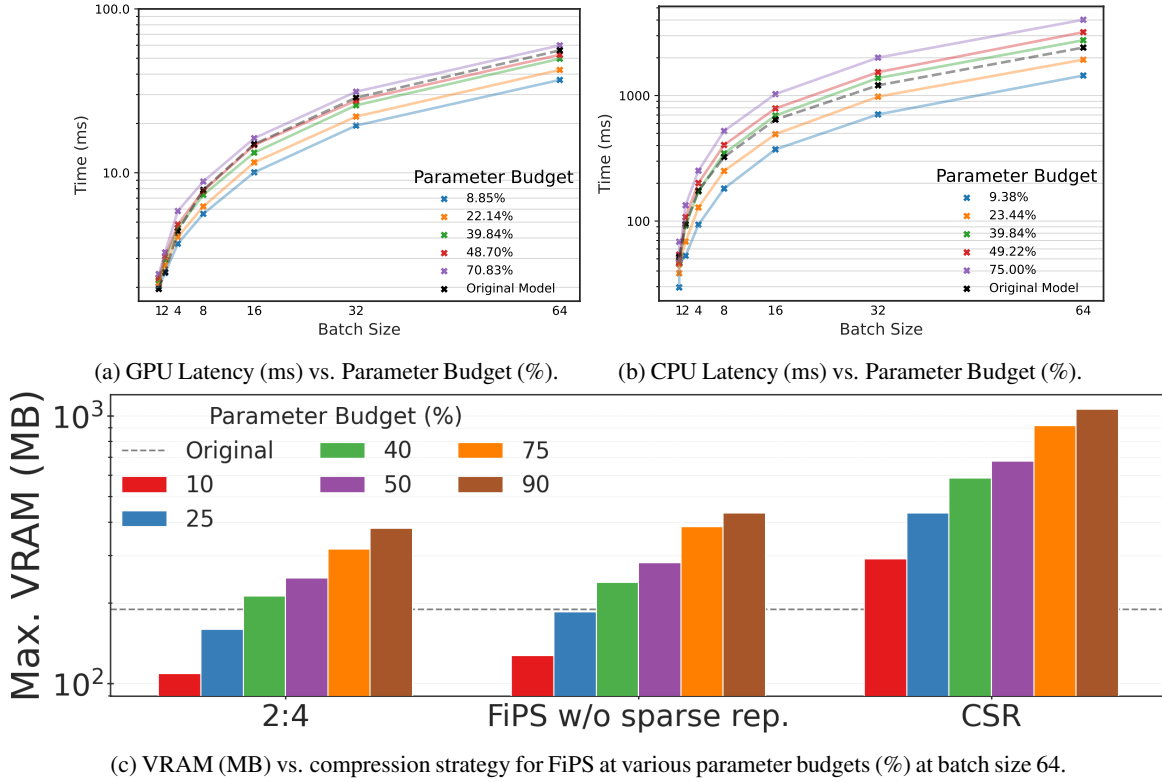


Figure 7: **DeiT-B Inference Latency and Memory Benchmarks.** (a) End-to-end latency of 2:4 sparse FiPS on an NVIDIA A4000 for batch sizes ranging from 1 to 64. FiPS with a 22% parameter budget exhibits a 25% latency improvement over the original network above batch sizes of 8. (b) Latency of 75% unstructured sparse FiPS accelerated with DeepSparse Engine on Intel Xeon W-2145 CPU. On CPU, FiPS with a 23% parameter budget is faster than the original network at all batch sizes measured. (c) Maximum VRAM allocation for 50% sparse FiPS using 2:4, strided (i.e., without a sparse representation), and Compressed Sparse Row (CSR) tensor storage. At 10 and 25% parameter budgets, 2:4 reduces maximum allocated memory by 44 to 18%, respectively. CSR increases memory overhead at this modest sparsity due to the associated overhead of storing the non-zero element indices. We find that the reduction in memory overhead is consistent for all batch sizes observed from 1 to 64. Note that all plots in fig. 7 have a logarithmic y-axis.